

B_0 shimming for in vivo magnetic resonance spectroscopy: Experts' consensus recommendations

Christoph Juchem¹  | Cristina Cudalbu²  | Robin A. de Graaf³  |
Rolf Gruetter⁴ | Anke Henning^{5,6} | Hoby P. Hetherington⁷ | Vincent O. Boer⁸ 

¹Departments of Biomedical Engineering and Radiology, Columbia University, New York, New York

²Centre d'Imagerie Biomedicale (CIBM), Ecole Polytechnique Fédérale de Lausanne (EPFL), Lausanne, Switzerland

³Department of Radiology and Biomedical Imaging, Yale University, New Haven, Connecticut

⁴Laboratory for Functional and Metabolic Imaging, Center for Biomedical Imaging, Ecole Polytechnique Fédérale de Lausanne, Lausanne, Switzerland

⁵Advanced Imaging Research Center, University of Texas Southwestern Medical Center, Dallas, Texas

⁶Max Planck Institute for Biological Cybernetics, Tuebingen, Germany

⁷Department of Radiology, University of Pittsburgh, Pittsburgh, Pennsylvania

⁸Danish Research Centre for Magnetic Resonance, Centre for Functional and Diagnostic Imaging and Research, Copenhagen University Hospital Hvidovre, Hvidovre, Denmark

Correspondence

Christoph Juchem, PhD, Associate Professor, Departments of Biomedical Engineering and Radiology, 351 Engineering Terrace, Mail Code: 8904, 1210 Amsterdam Avenue, New York, NY 10027.
Email: christoph.juchem@columbia.edu

Funding information

Centre d'Imagerie BioMédicale, Grant/Award Number: UNIL, UNIGE, HUG, CHUV, EPFL, and Leenaards and Je; SNSF, Grant/Award Number: 310030_173222/1

Magnetic resonance spectroscopy (MRS) and spectroscopic imaging (MRSI) allow the chemical analysis of physiological processes in vivo and provide powerful tools in the life sciences and for clinical diagnostics. Excellent homogeneity of the static B_0 magnetic field over the object of interest is essential for achieving high-quality spectral results and quantitative metabolic measurements. The experimental minimization of B_0 variation is performed in a process called B_0 shimming. In this article, we summarize the concepts of B_0 field shimming using spherical harmonic shimming techniques, specific strategies for B_0 homogenization and crucial factors to consider for implementation and use in both brain and body. In addition, experts' recommendations are provided for minimum requirements for B_0 shim hardware and evaluation criteria for the primary outcome of adequate B_0 shimming for MRS and MRSI, such as the water spectroscopic linewidth.

KEYWORDS

B_0 magnetic field, homogenization, shimming, spherical harmonic functions

1 | INTRODUCTION

In vivo magnetic resonance spectroscopy (MRS) provides biochemical information from living tissues and enables the noninvasive quantification of metabolic compounds based on spectral characteristics such as chemical shift and J-coupling. By contrast, magnetic resonance imaging (MRI) maps water content. MRS,¹ MRI and the combination of the two, MR spectroscopic imaging (MRSI),² share the need for homogeneity conditions of the static B_0 magnetic field in the object under investigation. In a recent consensus effort on proton magnetic resonance spectroscopic imaging, insufficient B_0 homogeneity was identified as the major limiting factor to more widespread clinical and research applications.³ In this paper, we summarize the most common concepts, techniques and algorithms of B_0 field correction, ie, shimming, and provide expert recommendations to realize optimal B_0 homogeneity. The reader is referred to the literature for the discussion of hardware and further details.⁴⁻⁶

2 | B_0 HOMOGENEITY AND SPECTRAL QUALITY

One of the major quality measures of MRS data that determines to what extent resonances from different molecules can be separated is the linewidth.⁷ If the linewidth relative to the spectral separation becomes too large, neighboring resonances cannot be distinguished (Figure 1).

Three components contribute to the experimental spectral linewidth: first, the natural line width of the metabolite signals determined by the life time of the spin states (T_2); second, line broadening due to microscopic intra-voxel B_0 field variations due to magnetic field variations on a molecular and cellular scale; and third, the macroscopic intra-voxel B_0 inhomogeneity due to large-scale susceptibility differences between different tissue types and air.⁸ Whereas the first two contributions are intrinsic and not under the control of the user, the third contribution is the only one that, in principle, can be removed through B_0 magnetic field shimming.

Details of the B_0 field distribution across the MRS volume of interest (VOI) define both spectral linewidth and lineshape, potentially leading to non-Lorentzian and even asymmetric spectral appearance. Lineshape effects can be reduced and spectral linewidths improved with postprocessing deconvolution techniques considering the underlying B_0 behavior.⁹ Nonideal signal shapes furthermore need to be accounted for during spectral fitting for quantification, for instance, by employing a Voigt lineshape model.¹⁰ However, lineshape distortions potentially reducing the MRS data quality and quantification accuracy can only be avoided through excellent B_0 field homogeneity during acquisition.

Regional specificity of the molecular and cellular environment results in varying intrinsic B_0 field conditions across different brain regions.⁸ Moreover, the macroscopic homogeneity varies largely due to variation in anatomy, and high-level B_0 field homogeneity is difficult to reach, for instance, in the frontal lobe above the nasal cavity and in the temporal lobes above the ear canals. As a result, some regional differences in spectral quality are expected even with the use of advanced B_0 shim approaches. Recent 3 T whole-brain MRSI data indicated that only ~ 75% of the voxels can be reliably analyzed due to B_0 shimming-related problems.³ Notably, higher spatial resolution for the parcellation of MRSI voxels in smaller subvolumes can be applied to reduce the macroscopic B_0 variation and frequency spread per spectrum if experimental sensitivity permits, a technique capable of improving spectral resolution without physical B_0 field correction.^{11,12}

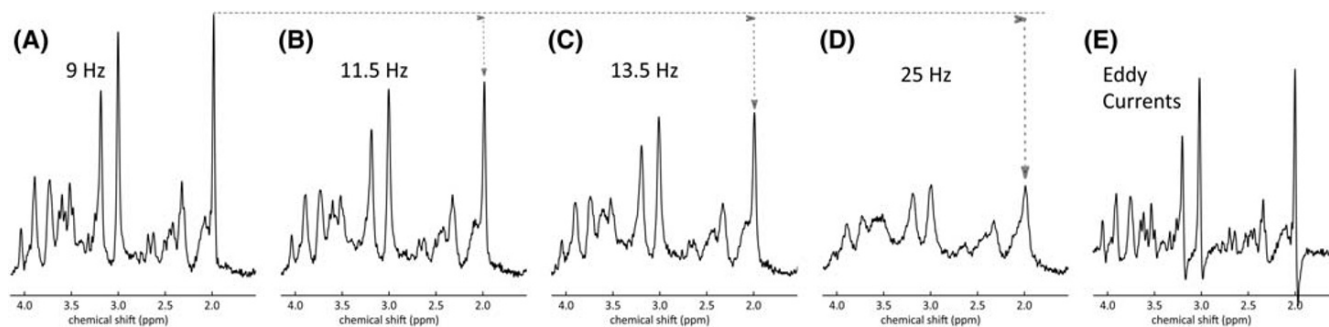


FIGURE 1 Example of 7 T prefrontal cortex (PFC) human brain spectra demonstrating different levels of shim quality that can be encountered: (A) excellent shimming (9 Hz linewidth) where most metabolites can be quantified with high accuracy; (B) adequate shimming where some SNR is lost (indicated with the arrow) and the fitting of some of the smaller resonances will be compromised; (C) acceptable shimming where more SNR is lost and especially small resonances are impacted more; and (D) poor shimming where a severe SNR loss is seen and even the major resonances cannot be measured accurately anymore. In (E) a spectrum with uncorrected residual eddy currents is shown. These effects are qualified as lineshape distortions, instead of linewidth changes

The global B_0 inhomogeneity across an entire organ or the field of view can limit the use of MRS and MRSI. This is because local field homogeneity is desired to achieve narrow linewidth for signals originating from the targeted MRS volume. At the same time, larger scale homogeneity is desired for optimal performance of frequency-selective radio frequency (RF) pulses for water suppression, lipid suppression or spectral editing across the MRS volume and beyond.^{13,14} Thus, MRSI in the frontal and temporal lobes remains challenging due to the necessity to obtain homogeneous B_0 conditions in these areas and their surroundings (Figure 1).

Lastly, residual eddy currents originating from the gradient or shim system can have a severe impact on the spectral quality (Figure 1E). Eddy currents primarily lead to temporal variations of the FID phase rather than a shortening of the T_2^* and distortions of the resulting spectral lineshape rather than increased linewidth. Deconvolution of the phase of the metabolite FID with the phase evolution from a corresponding high signal-to-noise ratio (SNR) water signal is a common approach to reduce lineshape distortions from eddy currents.¹⁵

3 | CONCEPT OF B_0 HOMOGENIZATION

3.1 | B_0 shimming hardware

Magnetic field B_0 homogenization, or shimming, describes the process of reducing its spatial variation by superposition of additional correction B_0 fields, which are realized using hardware elements called shim coils. In this paper we focus on the adjustment of B_0 homogeneity utilizing shim coils that provide B_0 field shapes resembling spherical harmonic (SH) functions. Such B_0 shim systems are widely available in current clinical systems. The magnetic field in the z-direction follows Laplace's equation, $\nabla^2 B_z = 0$. The solution of Laplace's equation can be expressed as a linear combination of SH functions, ie:

$$B_z(r, \theta, \phi) = \sum_{n=0}^{\infty} \sum_{m=-n}^n C_n^m r^n P_n^m(\cos\theta) e^{im\phi}, \quad (1)$$

where B_z is the magnetic field expressed in spherical coordinates r , θ and ϕ , C_n^m are weighting factors and P_n^m are associated Legendre polynomials of order n and degree m .^{5,16} With increasing order, n , the spatial complexity increases, providing greater ability to compensate for spatially complex variations. Every MRI system is equipped with a limited number of shim coils that are specifically designed to generate one of the low-order

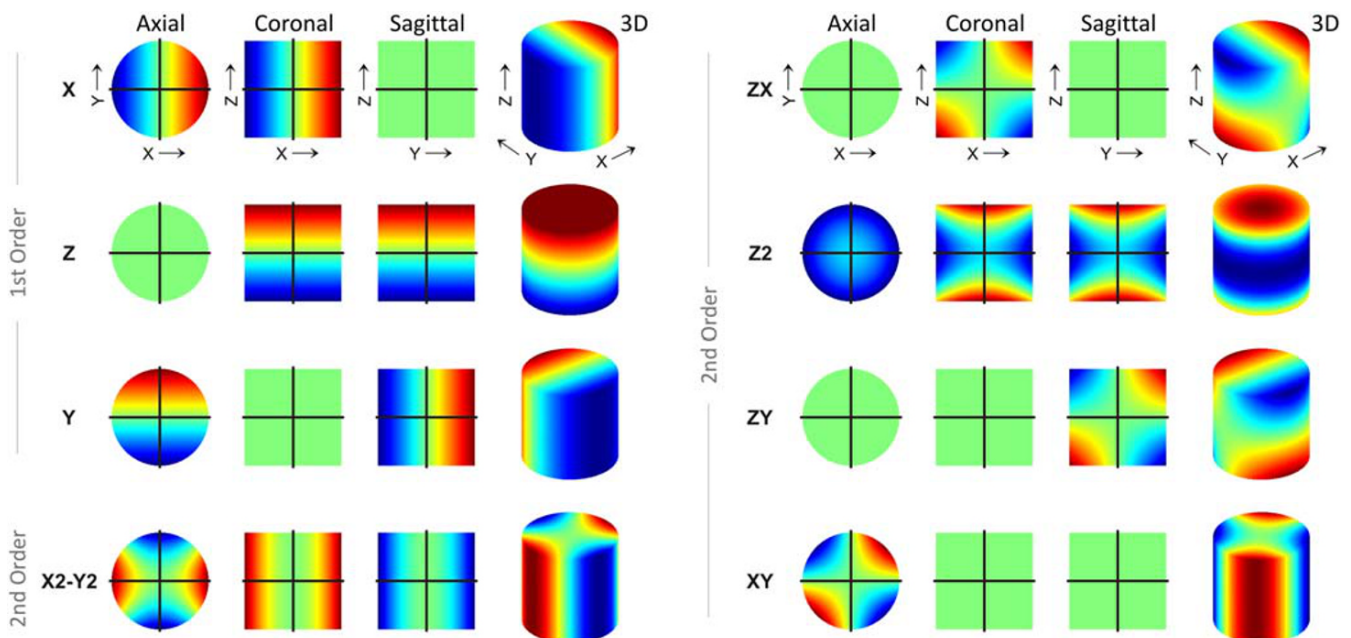


FIGURE 2 First- and second-order spherical harmonic (SH) shapes. SH functions are organized in orders n with $2n + 1$ terms per order. The single zero-order shape represents a global offset (not shown), and the three first-order terms describe linear field gradients identical to those applied for spatial encoding. Higher orders contribute shapes with higher-order symmetry and multiplicity and, therefore, can model progressively more complex target field shapes for improved compensation by B_0 shimming. For B_0 shimming, every SH shape is generated by a dedicated wire pattern and a shuffled multi-layer set of coils is employed as a SH shim system. Figure adapted from⁴

SH functions. We typically refer to the highest order present in a shim set to describe its hardware and shim capability, with the assumption that all shim terms of that order and below are present. Thus for a second-order shim system ($n = 0, 1, 2$) there are $1 + 3 + 5 = 9$ shims, ie: $(n + 1)^2$ shim terms, with $2n + 1$ different degree shim terms within each order (Figure 2). With the set of shim coils fixed, the process of shimming reduces to finding the amplitudes C_n^m in Equation 1 of each shim term that maximize the B_0 magnetic field homogeneity across the shim VOI. Traditionally, the coefficients C_n^m were determined by hand in an iterative procedure, cycling through the terms one at a time. Although it is possible to arrive at an optimal solution that way, nowadays faster, more robust and automated procedures have replaced earlier iterative approaches.

Recent advances have explored the use of both static and dynamic higher-order SH^{17–20} and nonspherical harmonic shim hardware,^{21–24} showing great benefit in achievable shim outcome. However, as this hardware is not widely available, this consensus effort focuses on static SH shimming with clinically available coil systems (Figure 2).

3.2 | Steps in the B_0 shimming procedure

The recommended B_0 shimming procedure (summarized in Figure 3) is based on, first, the acquisition of quantitative B_0 field information from the object under investigation (section 4), second, SH decomposition of the obtained B_0 information (Equation 1) and, third, conversion of the derived SH shim strength requirements to a set of actual shim coil currents (section 5). In principle, this analytical procedure needs to be executed only once, making B_0 shimming a single-step process and rendering iterations, either visible to the user or hidden in automated procedures, obsolete. In fact, with the use of suitable methods, optimal B_0 homogenization in a single shim adjustment should be the rule. Inaccuracies in any of the three steps of measurement, analysis and adjustment, however, can degrade the shim outcome. If the errors are relatively small, the repetition of the B_0 shim procedure can lead to an improvement in B_0 homogeneity. However, if imperfections are larger in nature, the B_0 homogeneity technically achievable with the shim system at hand might never be fully reached, or even become worse, despite iterations. Therefore, a recommended way to verify a B_0 shim procedure is to acquire a B_0 field map after shimming and validate the experimental shim outcome against the theoretically achievable, ie, predicted, B_0 distribution.

4 | METHODS FOR MAPPING B_0

4.1 | Signal phase as proxy for B_0 field

A one-size-fits-all approach is not applicable to B_0 shimming due to inter-subject variations in anatomy and subject positioning. Accurate mapping of the spatial pattern of the apparent field variation in the subject at hand is therefore necessary and a critical first step of the B_0 shim procedure. To date, the two most common methods to map B_0 inhomogeneity utilize either strategically designed one-dimensional (1D) projections along beams^{25,26} or full three-dimensional (3D) maps. Both of these methods are based on measuring (a minimum of) two acquisitions with different echo times (TE) in order to measure the signal phase evolution caused by the apparent B_0 magnetic field while removing phase offsets not related to the local magnetic B_0 field, for instance, the RF phase. For two-echo acquisitions, the difference in TE (ΔTE) results in a difference in phase, $\Delta\psi(x,y,z)$, between the two acquisitions of

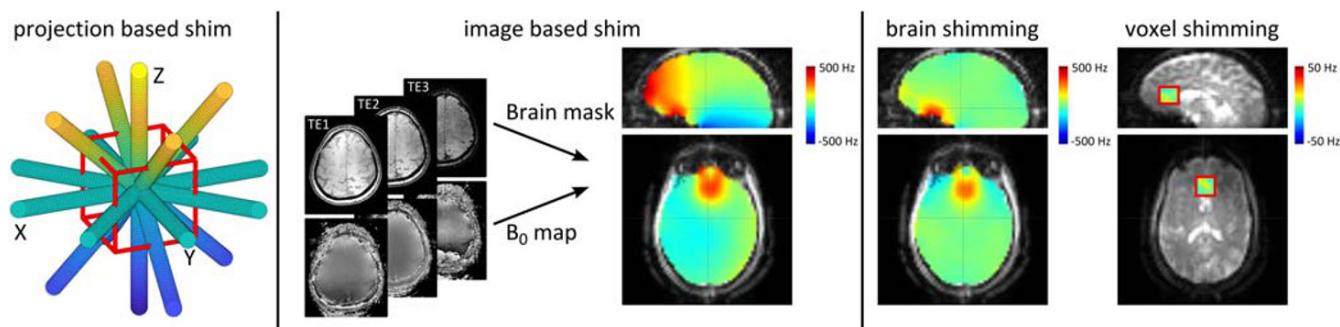


FIGURE 3 B_0 field information can be acquired by either projection-based methods (left) by acquiring field information along projections through the MRS voxel, or through image-based methods (middle) where multi-echo images of the target region are acquired. Here, the magnitude images are used for masking and the B_0 field map is calculated from the phase information. Image-based shim analyses (right) can consider and homogenize B_0 conditions across arbitrarily shaped volumes, including the whole brain, a single slice or small volumes for single-voxel MRS

$$\Delta\psi(x,y,z) = \Delta TE \cdot \gamma \cdot \Delta B_0(x,y,z), \quad (2)$$

where γ is the gyromagnetic ratio (rad/s/T). For small B_0 offsets the detected phase falls within the range $[-\pi \dots +\pi]$ and is directly proportional to the magnetic field offset, $\Delta B_0(x,y,z)$.

For larger ΔTE and/or larger ΔB_0 , the phase evolves beyond the $[-\pi \dots +\pi]$ range and the observed phase will then alias or wrap back into the $[-\pi \dots +\pi]$ range. Without correction, it will thus provide an incorrect value for the magnetic field offset, ΔB_0 . The most straightforward way to deal with phase wrapping is to reduce the echo time difference, ΔTE , potentially reducing the accuracy of the field estimate. When phase wrapping occurs, complex temporal and/or spatial phase unwrapping algorithms can be employed to detect and remove artificial phase wraps.²⁷⁻³⁰ The resultant continuous phase accumulation beyond the $[-\pi \dots +\pi]$ range then leads to accurate ΔB_0 estimates.

Alternatively, a sequence with more than two echoes, ie, TEs, can be used to have a combination of short and long ΔTE encoding times to provide large bandwidths for mapping (limited by the shortest evolution time used) while simultaneously providing high accuracy (limited by longest evolution time used). Although there is no clear optimum in the choice of echo times, highly accurate maps can be acquired from a combination of short and long TE, with sufficient bandwidth to preclude aliasing at the expense of increased acquisition time.⁵

Intrinsic to Equation 2 is the assumption that there is a single dominant resonance (ie, water), such that any variation in signal phase is directly proportional to the magnetic field offset. In the presence of multiple resonances with amplitude a_i , offset frequency Δf_i and relaxation time constant T_{2i} , as encountered, for example, in lipid-rich tissues, the signal at arbitrary TE can be derived from the sum S of the n individual signal components³¹

$$S(x,y,z,TE) = \sum_{i=1}^n a_i e^{-iTE \cdot (\gamma \Delta B_0(x,y,z) + 2\pi \Delta f_i)} e^{-TE/T_{2i}}. \quad (3)$$

For the brain, cerebral lipids are largely immobile and thereby show extremely short T_2 times making the assumption of a single dominant resonance (of water) valid. However, it has been demonstrated that the control of the B_0 homogeneity in the skull lipid area is beneficial to avoid lipid artifacts overlapping spectral lines of interest.³² For other organs, such as liver and skeletal muscle, both water and lipid components of the tissue have to be taken into account and a variety of methods have been developed to account for the differences in Larmor frequency between water around 4.7 ppm and lipids. The simplest approach uses “in-phase” TE that equals a multiple inverse of the water-lipid frequency separation according to $\Delta TE = n/\Delta f$. This assures that contributing water and lipid signals show the same phase behavior and the measured signal phase $\Delta\psi(x,y,z)$ is still directly proportional to ΔB_0 without additional modulation due to the frequency difference Δf . It is generally assumed that the lipid signal is dominated by the methylene lipid resonance at 1.3 ppm, and this is used for calculation of in-phase TE, where the water and lipid signal are in phase and B_0 mapping can be done. If more than one lipid resonance can be identified beforehand, this can be considered for enhanced B_0 accuracy (Figure 4).³³ Alternatively, more echoes can be used in combination with a more complex lipid signal model, such as the Dixon method or derivatives thereof, to provide high-quality B_0 maps even from lipid-rich tissues.^{34,35}

A complicating factor when relying on phase to estimate the B_0 field is that we do not account for other contributions to the phase during signal evolution (Equation 2). In practice, however, there can be several other sources of phase variation, the most important one being eddy currents generated by the switching of gradients in the B_0 measurement sequence. Care should be taken that this does not introduce a bias in the measurement. In practice, the resulting linewidth in MRS measurements is typically a useful indicator of the success of B_0 shimming. Alternatively, sequences can be run twice with opposite gradient polarity; after combining the data from the two acquisitions the eddy current component can be extracted and removed. However, the influence of eddy currents on B_0 field mapping is generally small and typically negligible.

4.2 | Projection-based mapping of B_0 magnetic field

Projection-based methods^{25,26} provide a highly efficient means to rapidly map the existing inhomogeneity using the symmetry of shims coils. In this class of methods, a spatially small 1D column or beam is excited and the position along the column is encoded by a read-out gradient. From Equation 1 we can see that the radial dependence and the angular dependence can be fully decoupled. By taking a straight column with fixed θ and ϕ through $r = 0$ (which can be defined as any point in the magnet), the magnetic field along projection j can be described by

$$B_j(r) = \sum_n k_{nj} r^n, \quad (4)$$

with $k_{nj} = \sum_{m=-n}^n C_n^m P_n^m(\cos\theta) e^{im\phi}$. Several strategically chosen columns can be chosen so as to provide a set of measurements that can uniquely resolve low (typically first and second) order shim contributions. Assuming that there is negligible variation across the cross-section of the column

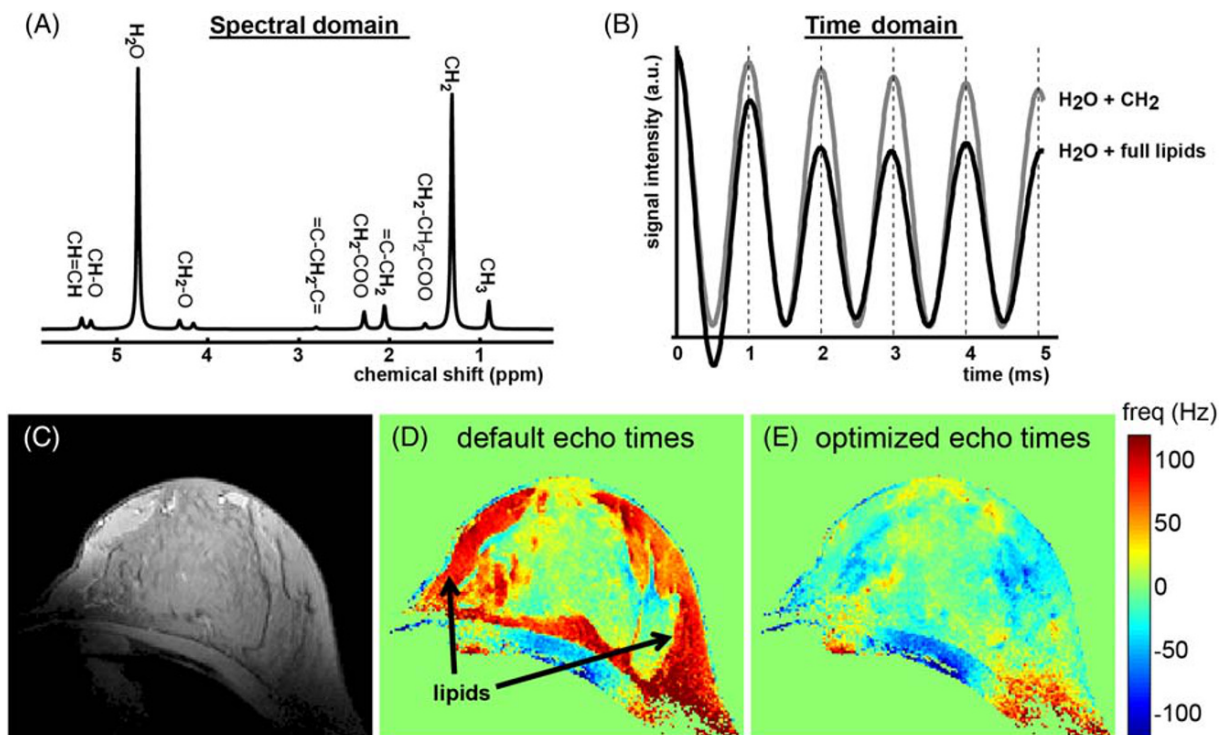


FIGURE 4 Simulated spectral (A) and time (B) domain signals of a combination of lipids and water. As a result of the presence of multiple resonances in the lipid spectrum, the time domain evolution shows a highly complex phase behavior when all peaks are taken into account. This affects the field estimation in the lipids in the breast (C). Therefore, the use of default in-phase TEs at 7 T ($TE_1/TE_2 = 2.96/3.95$ ms) based on the chemical shift difference of the major lipid resonance (CH_2) at 1.3 ppm versus water at 4.7 ppm results in erroneous field estimation in lipid tissue (D). Numerically optimized TEs ($TE_1/TE_2 = 2.92/3.94$ ms at 7 T) taking into account the measured 10 largest lipid resonances results in a flat phase response between lipid and glandular tissue (E). Reproduced with permission from³³

width (eg, typically ≥ 5 mm in human applications up to $\sim 25\%$ of the voxel size), the method reduces potential complications of phase unwrapping in the measured inhomogeneity to an easily solvable 1D problem. This in turn allows lengthy encoding times to increase sensitivity to small changes in frequency and maximize the accuracy of the maps. This “Fast, automatic shimming technique by mapping along projections” (FASTMAP) method obtains the information necessary to adjust the linear terms by measuring the field along at least three projections, and along at least six projections to determine all first- and second-order terms.²⁶ These and related techniques^{36–39} are rapid and efficient, especially when considering that multiple echoes can provide the reference measurement in the same excitation.^{36,40} Projection methods have proven to be highly successful for single-voxel MRS where the spatial extent of the target region or voxel enables the vast majority of the inhomogeneity present to be captured by first- and second-order SH fields. However, projection-based methods rely on a spherical region of interest (ROI) for shimming. For MRSI on whole slices, slabs or an entire organ, with a more complex shape of the shim VOI and the presence of relevant higher-order inhomogeneity, the usefulness of projection-based methods is limited.

4.3 | Image-based mapping of B_0 magnetic field

For larger shaped target volumes, like a whole slice, slab or the entire organ, image-based B_0 shimming is generally recommended.⁴¹ This is because the ROI is typically irregularly shaped, and this can be taken into account using image-based shimming. Also, for smaller ROIs, it might be essential to remove some areas such as air cavities or blood vessels from the shim ROI (see, for example, section 6.1).

For image-based shimming, 3D B_0 maps are typically acquired using a multi-echo gradient echo readout with two or more incremented TE delays to measure the field inhomogeneity as phase accumulation over time. Either multi-slice or 3D acquisitions can be used for this purpose.

Although there is no clear optimum for all applications, the highest spatial resolution is typically not necessary for B_0 shimming. For instance, in the human brain, moderate 2–3 mm in-plane and 2–4 mm through-plane resolution is sufficient for applications targeting tens or hundreds of cubic centimeter MRS/MRSI volumes. However, sufficient spatial coverage is advisable to have enough measurement points for numerically stable SH decomposition and shimming, as well as for proper delineation of the MRS target volume. Inter-slice gaps should be generally avoided to ensure sampling of the shim VOI is sufficiently dense, resulting in thousands or tens of thousands of points considered for the SH field fitting.

B_0 field mapping for shimming is naturally done at potentially inhomogeneous B_0 conditions and the underlying MRI sequence must therefore be robust against B_0 -induced artifacts. B_0 -sensitive techniques like echo planar imaging are therefore not recommended for use in B_0 mapping and conventional gradient-echo MRI at short TE, and high acquisition bandwidth is generally preferable to minimize the risk of phase wrapping and image distortions due to the unshimmed background field, respectively. There is a tradeoff with the use of high-amplitude readout gradients and large acquisition bandwidth, however, as image SNR is reduced and the potential for eddy current effects is increased. In the same vein, the slice excitation bandwidth should be large to minimize slice displacements. Parallel imaging seems to provide an efficient means of accelerating data acquisition for B_0 mapping as well; however, it is unclear to what degree introduced phase and magnitude errors can propagate as errors through the shim calculation.

After acquisition of the 3D B_0 field information, the shim VOI is manually or automatically delineated. Smaller shim VOIs can deliver improved shim performance, but the shim VOI should not become too small to retain both a favorable SNR and spatial coverage and therefore stay above ~ 15 mL for human applications. For single-voxel MRS, typically the MRS voxel is used as the shim VOI including a margin around the voxel to ensure stable numeric optimization and to reduce sensitivity of the shim result to motion and localization imperfections. For example, a $25 \times 25 \times 25$ mm³ shim VOI could be used for a $20 \times 20 \times 20$ mm³ MRS voxel. For brain MRSI, automated brain segmentation tools can be used⁴² to provide a mask of the brain. This brain mask can be intersected with the MRS/MRSI excitation volume, potentially including a certain margin. Also, manual delineation can be used to define the most optimal VOI for shimming, but is not recommended due to the user variability and time constraints. See section 7 for further details and recommendations.

5 | SHIM CALCULATION AND CROSS-TERM CORRECTION

Once the B_0 field information in the shim VOI has been measured either along projections or using image-based mapping, the respective currents in the individual shim coil elements (each responsible for generating a different SH shape) need to be calculated by decomposing the measured B_0 field variations within the shim VOI into the separate SH shim field components. This should be done with a constrained numerical minimization that takes the shim amplifier limits into account. Regularization can be employed to reduce the sensitivity to noise, especially if very high orders are used.

The most straightforward way to calculate the shim coil settings is a direct fitting using as basis fields the SH decomposition of the B_0 inhomogeneity to the theoretical coil strengths from Equation 1 according to:

$$\begin{aligned} & \underset{\mathbf{l}}{\text{minimize}} \|\mathbf{B}_0 - \mathbf{S}\mathbf{l}\|_2^2 + \lambda \|\mathbf{l}\| \\ & \text{subject to } -I_{\text{limit}}[i] \leq \mathbf{l}[i], i = 1, \dots, N, \end{aligned} \quad (5)$$

where \mathbf{B}_0 is a vector containing the measured magnetic field in the voxels in the ROI, \mathbf{S} is a matrix containing the description of the analytical SH fields in the ROI, \mathbf{l} is a vector with strengths for the individual SH shapes and λ is an (optional) regularization factor.

This assumes that B_0 fields generated by individual coil wire patterns are pure and truly independent (ie, orthogonal). However, most shim coils also produce unwanted (cross-) terms along with the primary shape, ie, the self-term. The effective field shape produced by a shim coil can therefore be considered a combination of the desired B_0 shim field and a secondary field distortion due to cross-terms. When ignored in the calculation of B_0 shim strengths, the latter imperfections lead to nonoptimal magnetic field homogeneity and one or more readjustments or refinements, ie, iterations, can be required for their cancelation. These additional steps can be avoided by taking both self- and cross-terms into account in the original shim strength calculation. The derivation of SH shim strengths, \mathbf{s} , considering both self- and cross-terms, is achieved by multiplication of the vector \mathbf{l} comprising the fitted pure SH field components in the considered VOI, with the inverse of the shim coil calibration matrix \mathbf{A} .¹⁷

$$\mathbf{s} = -\mathbf{l} \cdot \mathbf{A}^{-1}. \quad (6)$$

This method works as long as the imperfections, regardless of order and degree, are included in the models of the fields generated by individual shim coils. An approach to derive this coupling matrix \mathbf{A} is described in the next section.

5.1 | Calibration of shim coil systems

In principle, the B_0 field shapes provided by a shim coil system should follow the theoretical description in Equation 1. However, already in the design process it is clear that coils that provide these pure terms over large regions of space are hard to create. Even though the generated magnetic field could be derived by theoretical Biot-Savart simulation from the employed wire patterns, nevertheless, manufacturing imperfections

and installation tolerances will affect the obtained field shapes and coil sensitivities. In addition, other aspects of the shim coil operation, for example, the employed amplifier hardware, can influence its performance.

Because of these considerations, a per-system experimental calibration of the shim coils is generally recommended, as incomplete knowledge of the shim fields results in systematically degraded B_0 shim outcome. Notably, shim systems need to be calibrated only once as long as the coils and amplifier hardware are not altered, as coil geometries are fixed inside the magnet bore and B_0 field shapes are not affected by the subject under investigation (as opposed to RF, or B_1 , shimming). This calibration information can then be used for all subsequent shim calculations irrespective of target B_0 shim VOI and intended MRS application.

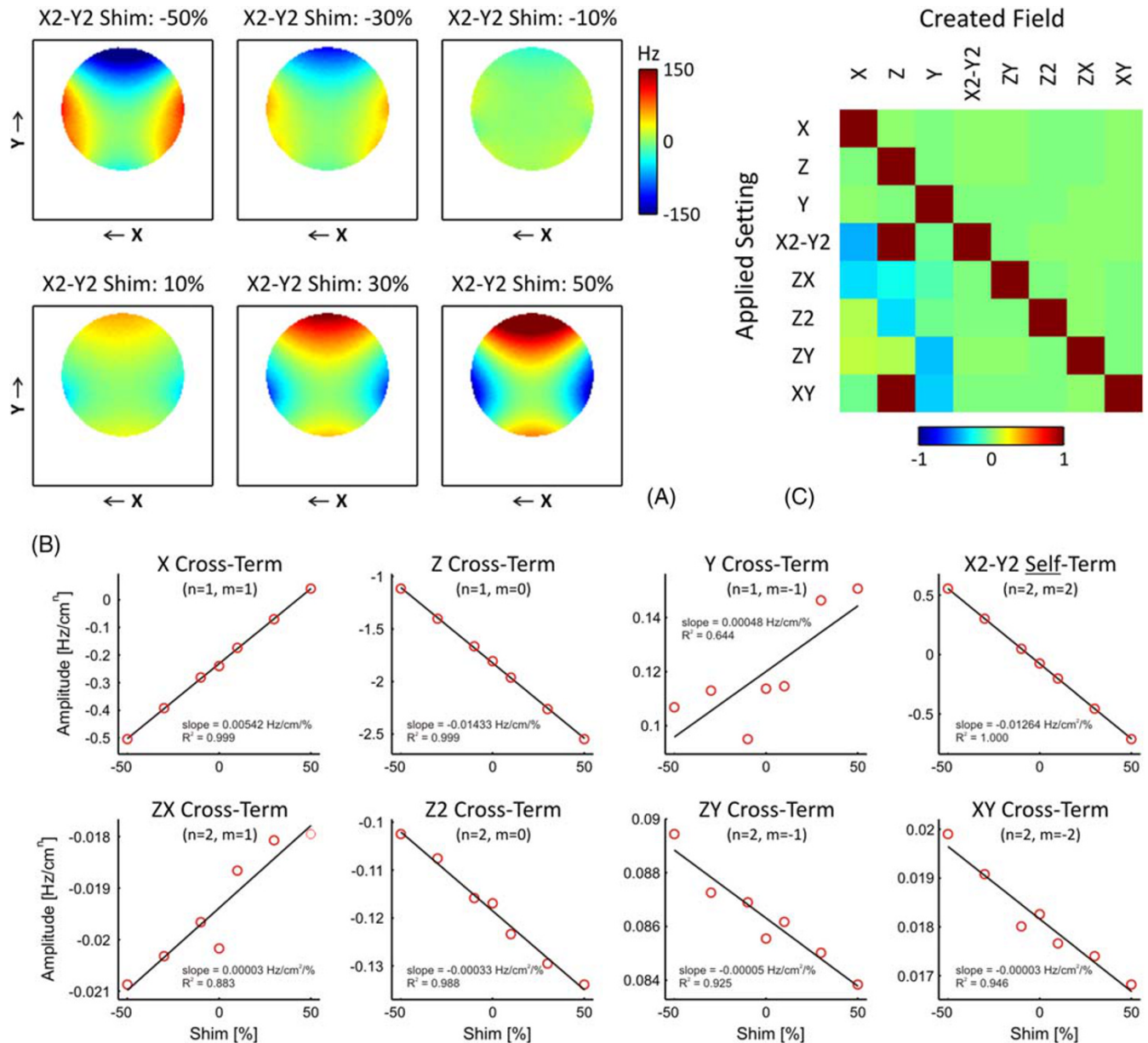


FIGURE 5 Example calibration of a spherical harmonic (SH) coil system of a clinical 3 T MR system (General Electric, Discovery MR750).

(A) The experimental calibration of an individual coil (here X2-Y2) is achieved by mapping the B_0 field for a selection of shim strength settings and SH decomposition of the obtained B_0 field shapes. (B) Linear regression of the X2-Y2 amplitude produced per unit current (or shim setting), ie, the slope of the curve provides the sensitivity of the coil's self-term and allows the translation of shim amplitudes (in Hz/cmⁿ) to coil currents (eg, % of maximum [A]) and vice versa. Cross-terms generated by the X2-Y2 coil, ie, its imperfections, are derived by linear regression of the determined amplitudes from other SH shapes against the X2-Y2 shim settings. Note the reversed polarity of the shim field generated by the X2-Y2 coil, significant X and Z cross-terms and much smaller (note the difference in scale) cross-terms resembling Y and other second-order shapes. (C) Analogous repetition of this analysis for the remaining coils of the SH shim system results in a 8 x 8 coil calibration matrix for the second SH order shim system at hand that comprises the full characterization of the coil systems' self- and cross-term sensitivities (located at diagonal and off-diagonal positions, respectively) up to the supported SH shim order, here plotted as the normalized slopes

Calibration of a B_0 shim system is achieved by sampling field maps of each of the shim coils at a variety of shim settings (Figure 5). The attained field maps are decomposed into SH terms up to the order of the shim system. Linear regression of the applied shim strengths and the fitted SH coefficients (eg, in Hz/cmⁿ) is then used to derive the calibration matrix A comprising the desired effects of all shim channels as self-terms along the diagonal axis along with the undesired field components of a coil resembling any of the other SH shapes supported by the shim system, ie, their cross-terms, encountered in the off-diagonal positions.

5.2 | Shim calibration: experimental setup and further recommendations

Calibration experiments of a shim system are generally performed on phantoms. The phantom should be reasonably large (eg, diameter > 15 cm for human MR systems), have a single resonance (eg, water), show continuous signal throughout the volume (ie, avoiding resolution phantoms with internal structures) and possess favorable T_1 and T_2 characteristics for the calibration scans, for instance resembling in vivo conditions. A basic B_0 preshim of the phantom is not technically necessary, but advisable to minimize background image deformation and signal cancelation.

The risk of phase wrapping is higher during calibration compared with B_0 conditions encountered in typical in vivo applications. Therefore, the shortest delay between echoes has to be selected such that phase wraps are minimized. It is recommended to use at least four echoes, for instance using echo time increments of 0.25/1/3 ms. This covers a frequency range of ± 2 kHz with high accuracy. Furthermore, the readout bandwidth should be chosen to be large (ie, 100 kHz or more) to minimize B_0 -induced spatial misregistration and signal loss when running high calibration shim settings. On the other hand, the SNR should remain sufficient to allow reliable phase estimates and, if significant, induced eddy currents should be mitigated by signal averaging of B_0 maps acquired with opposite gradient polarity. A calibration analysis should be performed that is based on six or more individual shim settings per coil, thereby allowing both reliable regression analysis and quality assessment (Figure 5).

Thorough quality assessment of both B_0 field maps and the calibration analysis is highly recommended to avoid systematic errors. It is generally advisable to reject voxels with erroneous or even suspicious field behavior. The average error of the slope calculation for the self-terms should be well below 1%, as a consistency measure for a high level of linearity of the shim experimentation (eg, amplifier linearity), data reconstruction (eg, image artifacts) and calibration analysis (eg, system setting errors).

6 | CHALLENGES AND PITFALLS OF B_0 SHIMMING

Each step of the B_0 shimming process comprising measurement, analysis and adjustment has potential for specific artifacts, errors and sub-optimal choices that need to be recognized in order to arrive at the highest possible B_0 magnetic field homogeneity for the shim system at hand, in the easiest and most robust way.

6.1 | Acquisition of B_0 magnetic field maps

According to Equation 2, B_0 field information is calculated as the rate of phase evolution per unit time.⁴ The color-coded image in Figure 6B is referred to as a B_0 map and provides a quantitative measurement of the magnetic field B_0 offset (in Tesla [T], Hertz [Hz] or parts-per-million [ppm]) at each spatial location, or pixel. However, the B_0 map is almost always compromised by a number of artifacts, of which a few are indicated in regions 1-4 in Figure 6B. Whereas the majority of the B_0 map is varying smoothly, regions 1-4 indicate areas where the magnetic field homogeneity appears to change by hundreds of Hz between pixels. The underlying artificial phase values can originate from several sources, which should be addressed in different ways. In region 1, pixels at the edge of the brain have artifactually fluctuating B_0 values due to low SNR in the underlying MR image (Figure 6A). A signal intensity threshold can be used to remove such pixels. The negative offset in the blue pixels in region 2 should actually have a positive offset. However, these pixels appear with an incorrect offset due to phase wrapping. This effect can be minimized by adjusting the B_0 map acquisition to shorter echo spacing⁴³ or by numerically unwrapping the B_0 map. Regardless of the solution, phase wraps have to be removed before continuing with B_0 map analysis and shim strength calculation. Some pixels in region 3 also appear to have artificial B_0 values. This is due to flowing spins in the sagittal sinus vein and cerebral spinal fluid compartment resulting in wrong phase values. Also, these pixels should not be considered and excluded from the analysis. Finally, in region 4 and essentially the entire skull region, large variations in magnetic field offset can be observed due to the presence of extracranial lipid signals. These pixels can either be removed by skull stripping or improved by adjusting the B_0 field map acquisition (Equation 3). Further shim VOI selection can entail a number of steps related to signal thresholding, removal of pixels with unrealistically steep local gradients, single "island" pixels and excessive offset values. The final masked B_0 map (Figure 6C) should only contain magnetic field offset values with a high degree of certainty regarding their validity. The masked B_0 map in Figure 6C could be used to homogenize the entire slice as used in, for example, MRSI.

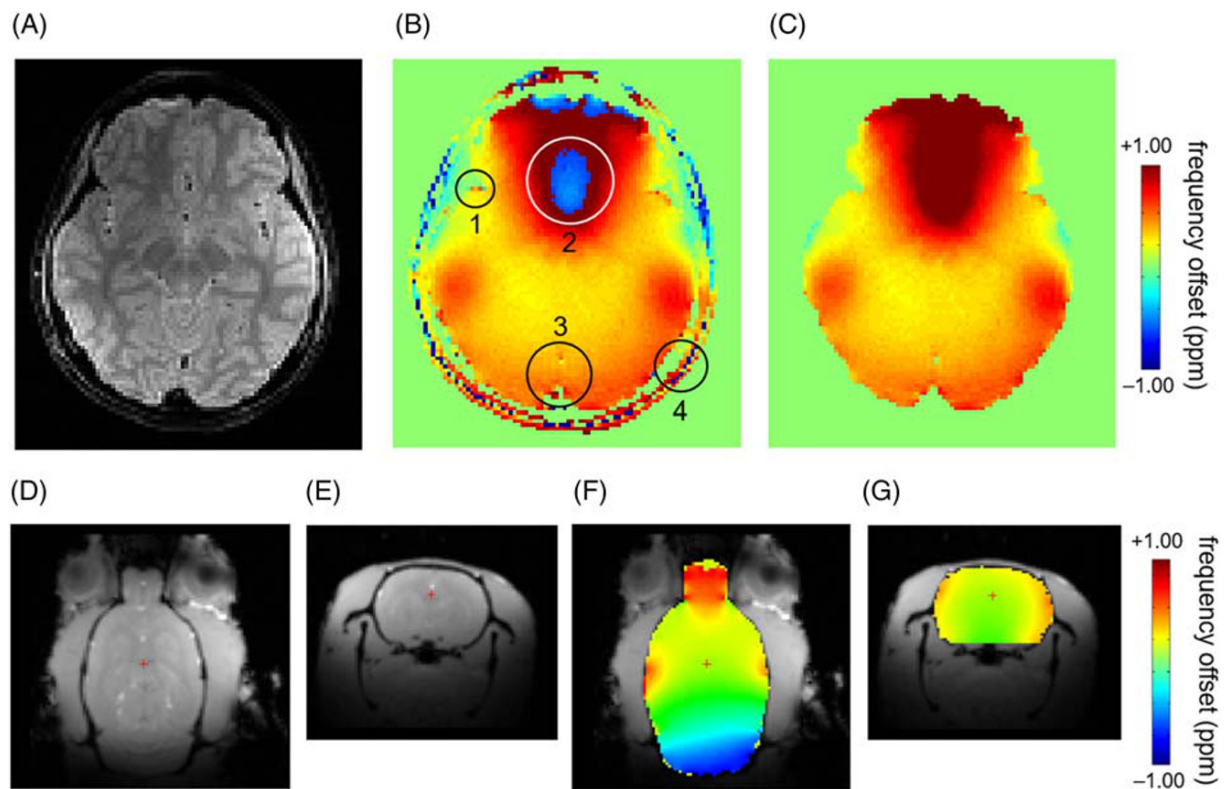


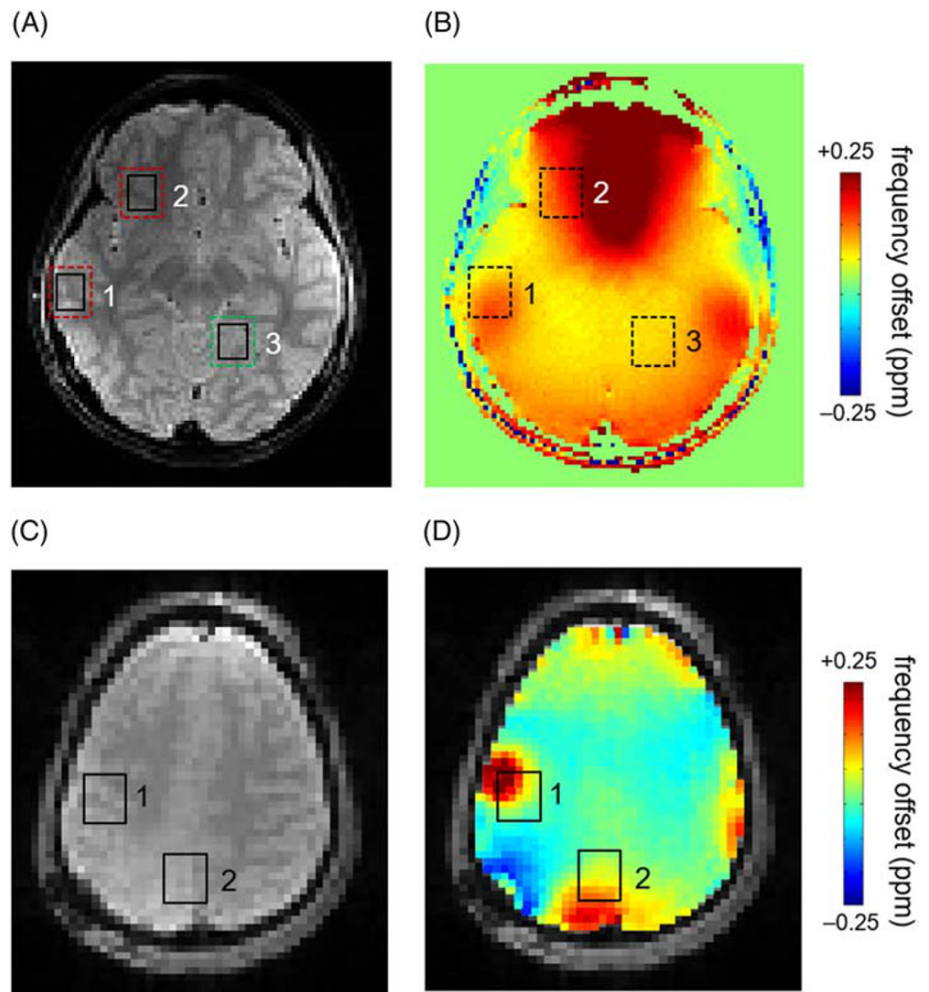
FIGURE 6 (A) Anatomical MRI and (B) quantitative B_0 map from the human brain in vivo. The regions 1-4 in (B) indicate a variety of artifacts that need to be removed to yield a reliable B_0 map of the human brain (C). (D, E) Anatomical MRI from a rat brain in axial and sagittal view and (F, G) segmented and overlaid B_0 map from the rat brain

In the same vein, B_0 shimming of the rodent brain (Figure 6D,E) relies on meaningful brain segmentation in combination with accurate B_0 field mapping (Figure 6F,G). Once quality control has been applied and the remaining potentially erroneous pixels have been excluded (eg, yellow data points in the posterior brain and at the tip of the olfactory bulb; Figure 6F), one can safely proceed with B_0 field analysis and the computation of optimized shim fields.

6.2 | Challenges and limitations of B_0 shimming

From Figure 6 it should be clear that a quantitative B_0 map reveals important information about regional B_0 magnetic field behavior, potentially challenged by local artifacts that are not apparent on MR images. However, on most MR platforms, and especially for single-voxel MRS, the selection of shim VOIs is purely based on geometry extraction from (anatomical) MR images without consultation of the underlying phase behavior and quality metrics of the derived B_0 maps. This can have important consequences regarding the achievable magnetic field homogeneity and the resulting data quality. In Figure 7A,B, three potential locations for single-voxel MRS are indicated. MRS VOI 3 is placed centrally away from major magnetic field inhomogeneity gradients and is likely to provide high-quality MRS data. Even when the spatial resolution of the B_0 map is relatively coarse (eg, 5 mm), the shim VOI margin around MRS VOI 3 can be extended without much consequence to include more B_0 map pixels for a more accurate estimation of the magnetic field. MRS VOI 1 is placed close to the edge of the brain. In this case, a simple extension of the margin around MRS VOI 1 would be disastrous as the larger VOI now includes artifactual values from the skull region. Hence it is recommended to intersect the shim VOI with a skull-stripped B_0 map to limit the fitting to only brain tissue, or to adapt the B_0 mapping to improve field estimation in the lipid-rich tissue (Equation 3). MRS VOI 2 has a similar problem in that extending the margin will include higher-order magnetic field gradients that may be incompatible with the available low-order SH shims. Exact placement of MRS VOI 2 with respect to the frontal magnetic field disturbance and minimizing the VOI extension can make the difference between good and unacceptable MRS data quality. None of these considerations can be properly judged from the anatomical MR image alone. The magnetic field homogeneity in the upper parts of the brain (above the ventricles) is high due to the absence of magnetic susceptibility boundaries and voxel locations can generally be selected based on the anatomical MRI. However, while the anatomical MRI in Figure 7C is artifact-free, the corresponding B_0 map in Figure 7D indicates strong, local magnetic field inhomogeneity. This is due to the presence of postsurgical metal clips in the skull. In this case the success of shimming becomes critically

FIGURE 7 The added value from voxel planning on a B_0 map is displayed by three example voxel locations as indicated on an anatomical MRI (A) and a quantitative B_0 map (B) from a healthy subject. Two more example voxel locations are displayed on an anatomical MRI (C) and quantitative B_0 map (D) from a subject with postsurgical metal clips in the skull



important based on the exact MRS VOI location, and a tradeoff is to be made between MRS VOI location and MRS VOI size in relation to the underlying B_0 field.

7 | COMPUTATION AND ADJUSTMENT OF B_0 SHIM FIELDS: MINIMUM STANDARDS AND FURTHER RECOMMENDATIONS

7.1 | Shim volume selection

The volume considered for B_0 shimming typically resembles the MRS target region, but can differ as long as the characteristics of the B_0 distribution to be homogenized are properly captured. For single-voxel MRS using relatively small voxels, good linewidths can be achieved across most areas in the human brain (see Table 1 for guideline values). A moderate extension of the shim VOI beyond the voxel is useful to minimize planning mismatches and sensitivity to small subject motion (eg, using a $25 \times 25 \times 25 \text{ mm}^3$ shim VOI for a $20 \times 20 \times 20 \text{ mm}^3$ voxel). The extension of the shim VOI should, however, be used with care, as it rests on the assumption that the B_0 distribution in the vicinity of the original shim VOI resembles the shapes encountered within the MRS voxel. A moderate shim VOI extension can therefore be applied if B_0 conditions can be expected to change slowly, but must be avoided in areas of severe local B_0 gradients or at the brain surface if no further quality and selection measures (eg, SNR threshold) are applied (eg, Figure 7B, voxel 2). When very small MRS voxels are used, the shim VOI is best kept above $\sim 15 \text{ mL}$ for human applications to ensure a sufficient number of data points and spatial coverage for meaningful SH decomposition.

For MRSI, full B_0 maps with 3D coverage are generally recommended for B_0 shimming. Best practice is to adapt to the actual shape of the object under investigation, for example, the brain, and intersect that with the MRSI volume. A multi-slice optimization can provide significantly better results than whole-brain optimization, but running an interleaved multi-slice MRSI sequence will require the higher-order eddy currents to be corrected for.⁵ This is not implemented on most systems.

TABLE 1 Summary of attainable B_0 shim quality expressed as linewidths of the real part water spectrum in humans as a function of scanner B_0 field strength (1.5, 3 and 7 T) and body parts for typical single-voxel acquisitions. Note that this table is for basic orientation only. Further potentially relevant details are omitted here as they are beyond the scope of this paper

B_0	Anatomical region	Excellent FWHM, Hz	Adequate FWHM, Hz	Acceptable FWHM, Hz	References
1.5 T	Brain	3-4	5-6	7-8	53
	Brain (PFC)	3-4	5-7	8-10	
	Breast	6-10	11-15	16-20	54
	Heart	7-9	10-12	13-15	55,56
	Liver*	13-15	16-18	19-22	
	Prostate	3-4	5-7	8-10	57
	Skeletal muscle	4-5	6-7	8-10	58,59
3 T	Brain	5-6	7-8	9-10	60
	Brain (PFC)	5-7	8-10	11-13	39,61
	Breast	12-18	19-24	24-30	54
	Heart	9-13	14-18	19-23	62-64
	Liver*	18-23	24-29	30-35	65,66
	Prostate	5-7	8-10	11-13	67
	Skeletal muscle	8-10	11-13	14-16	59
7 T	Brain	9-10	11-12	13-14	50
	Brain (PFC)	9-12	13-15	16-19	4,50
	Breast	20-30	31-40	41-50	33
	Heart	16-21	22-26	27-33	
	Liver*	30-39	40-49	50-60	68
	Prostate	9-12	13-15	16-19	69
	Skeletal muscle	12-15	16-19	20-24	59,70

For single-slice MRSI, an additional margin should be taken into account in the slice direction to adequately capture through-slice B_0 imperfections. At least three slices of a B_0 map, spanning a narrow 3D slab should be considered to avoid shim degeneracy, ie, loss of uniqueness, and to assure numerically stable results.

For both MRS and MRSI, it can be advantageous to include surrounding tissue such as the skull lipid or the tissue surrounding the prostate into the shim problem as a second ROI to control the frequency offsets outside the main target area. This can minimize lipid bleeds, improve water suppression and reduce the influence of subject motion.^{32,44}

7.2 | Shim field constraints

The B_0 shim outcome is similarly impaired if the strength of the required shim field exceeds the capacity of the available coil system and amplifier electronics. In such a case, the shapes can be reproduced with the available B_0 shim system, but the dynamic range appears insufficient for their compensation and inevitable residual imperfections remain. Shim algorithms should robustly converge in the presence of shim field constraints, nonorthogonal shim coil fields and under characteristic SNR and artifact content of the B_0 maps. Shim field constraints have to be taken into account to generate a shim set that makes optimal use of the available hardware configuration.⁴¹ If SH amplitudes encountered in the shim volume exceed the technical ability of the shim system at hand, a clear warning should be issued informing the user that the dynamic range of one or more channels of the employed shim hardware is exceeded. However, it goes without saying that final current demands to the shim amplifier hardware must remain within the available amplitude constraints at all times.

7.3 | Subject movement

The minimization of B_0 inhomogeneity by static B_0 shimming as outlined above rests on the assumption that B_0 conditions do not change between B_0 mapping and the end of the MRS/MRSI acquisition. Subject movement can result in varying B_0 conditions and therefore needs to be minimized by appropriate measures such as padding, regular verbal encouragement and limited study duration. Although technically feasible, the discussion of real-time motion and B_0 correction^{45,46} is beyond the scope of this paper.

8 | RECOMMENDATIONS FOR ANATOMY-SPECIFIC B_0 SHIM STRATEGIES FOR SINGLE-VOXEL MRS AND MRSI

8.1 | Human brain

Due to the small extent of the target region (1-3 cm on a side) in single-voxel acquisitions, excellent results have been achieved in the brain using second-order shims.⁸ This forms the basis for most clinical MRS applications. SH shapes beyond second order can provide improved B_0 shim outcomes, especially for challenging single-voxel regions such as the frontal lobe.^{4,5} For MRSI, B_0 conditions need to be homogenized in thick individual slices (~10 mm), in slabs (eg, 4-6 cm) or across the entire brain. Progressive improvements are expected with increasing order beyond second-order shimming, the extent of which is highly dependent on the spatial extension of the considered region-of-interest in combination with compressed B_0 field challenges, for instance, in the prefrontal cortex (PFC) or the medial temporal lobes.^{17,18}

8.2 | Human breast

With single-voxel MRS in the breast, it is important to take note of the large field variations induced by interfaces between lipids, tissue and air due to their differences in magnetic susceptibility. The voxel is best placed fully inside a homogeneous area to achieve optimal shim performance. In lipid-rich tissue, the lipid peak might be higher than the water line, or a third peak could be present from possible silicone implants. This may lead to an erroneous determination of the water frequency and an unintended shift of the MRS voxel. Adjustment of the water resonance frequency might be necessary prior to and after B_0 shimming. Respiratory triggering might be considered as the breathing-induced field changes in the breast can be significant.⁴⁷

8.3 | Human prostate

The prostate gland is a relatively homogenous organ and good field homogeneity can commonly be reached both in single-voxel MRS and in MRSI. A confounder in 3D MRSI of the complete gland can be the presence of rectal gas close to the prostate, which can strongly influence the field homogeneity in the peripheral zone of the prostate. Motion can be mitigated with antiperistaltic drugs. The gland is typically surrounded by lipid-rich tissue, leading to a loss of shimming quality close to the lipid interface.

8.4 | Human liver

For the liver it is recommended to place the voxel away from the edges and large vessels. As the liver moves with respiration, B_0 mapping in particular should be synchronized with the breathing cycle, or performed in breath hold. The MRS acquisition can also be acquired in synchrony with breathing, but this might lead to prolonged scan times. Alternatively, retrospective data rejection can be used to remove spectra corrupted by varying B_0 conditions due to motion.

8.5 | Human heart

Cardiac MRS is typically performed on single voxels placed in the septum, thereby preventing lipid contamination. Cardiac triggering is best used for both B_0 mapping and MRS data acquisition. Respiratory motion compensation can be performed by breath holding, triggering, or retrospective data selection. While higher-order shimming can remove more complex field inhomogeneity, it might be less robust against movement when no triggering is applied.

8.6 | Human skeletal muscle

Voxel placement has to be done in a way to avoid fascia to minimize extramyocellular lipid contamination. The ΔTE step has to be chosen such that water and lipids are in phase. In lipid-rich tissue, the lipid peak might be higher than the water peak, potentially leading to erroneous frequency determination and unintended voxel shifts. Frequency adjustment of the water peak might be necessary prior to and after B_0 shimming.

8.7 | Rodent brain

B_0 shimming for preclinical MRS is usually performed on even smaller VOIs (1-3 mm on a side for a specific brain region) due to the smaller size of the brain.⁴⁸ While complex susceptibility-induced B_0 field distortions are apparent in the mouse brain, first- and second-order SH shimming has been shown to provide excellent B_0 homogeneity in any brain location and narrow line widths with single-voxel MRS if the dynamic range of the shims is large enough.⁴⁹ The lowest linewidth can be achieved from more homogeneous regions deeper inside the brain, such as hippocampus and striatum (see Table 2). This intrinsic linewidth limit in the mouse hippocampus is not achieved in other brain regions due to internal structure (eg, cerebellum⁴⁸) or macroscopic B_0 shim challenges (eg, near the brain surface). Due to the difference in anatomy and typical voxel sizes and locations, the generally achievable linewidths in the rat brain are ~ 5%-10% lower for any given B_0 field strength compared with equivalent brain regions in mice (Table 2).

9 | RECOMMENDATIONS FOR TARGETED B_0 SHIM OUTCOME AND QUALITY MEASURES

9.1 | Shim hardware requirement

Higher-order field contributions become progressively less relevant the smaller the considered shim VOI, and for single-voxel MRS narrow linewidth can mostly be achieved using strong first- and second-order SH shims. In some challenging locations like the frontal lobe in the human brain, there can be significant higher-order field contributions and including strong third-order shim terms can provide significantly enhanced shimming. Whole-brain field optimization typically requires less strong, but higher-order SH field shapes for a good field compensation.

Table 3 summarizes approximate required hardware capabilities of SH shim systems for B_0 homogenization in the human and rodent. Required SH shim amplitudes vary between body regions. The table therefore focuses on localized B_0 shimming of the more challenging shim areas such as single-voxel MRS in the PFC, which demand SH field shapes of higher amplitude.

9.2 | Quality metrics and spectroscopic linewidths

Achievable linewidths (full width at half maximum [FWHM]⁷) are a function of the scanners' B_0 field strength and spectral lines appear broader at higher field strength.⁸ An effective gain in spectral resolution and dispersion at higher field strength is therefore only achieved if the increased

TABLE 2 Summary of attainable B_0 shim quality expressed as linewidths of the real part water spectrum in rat and mouse brain as a function of scanner B_0 field strength (9.4, 11.7 and 14.1 T) in different brain locations for typical single-voxel acquisitions. Further potentially relevant details are omitted here as they are beyond the scope of this paper. Although possible, some care should be taken to interpolate or extrapolate these numbers to different field strengths. Note that this table is for basic orientation only

B_0	Rat/mouse	Brain region	Excellent, Hz	Adequate, Hz	Acceptable, Hz		
9.4 T	Rat brain ⁷¹⁻⁷⁶	Hippocampus/striatum	9-10	11-12	13-14		
		Cerebellum	14-15	16-17	18-19		
		Cortex	11-12	13-14	15-16		
	Mouse brain ^{49,77,78}	Hippocampus/striatum	10-11	12-13	14-15		
		Cerebellum	15-16	17-18	19-20		
		Cortex	12-13	14-15	16-17		
		11.7 T	Rat brain ^{75,79-81}	Hippocampus/striatum	13-14	15-16	17-18
				Cerebellum	18-19	20-21	22-23
				Cortex	14-15	16-17	18-19
Mouse brain ^{82,83}	Hippocampus/striatum	14-15	16-17	18-19			
	Cerebellum	18-19	20-21	22-23			
	Cortex	15-16	17-18	19-20			
14.1 T	Rat brain ^{84,85}	Hippocampus/striatum	16-17	18-19	20-21		
		Cerebellum	20-21	22-23	24-25		
		Cortex	17-18	19-20	21-22		
	Mouse brain ⁸⁶⁻⁹⁰	Hippocampus/striatum	18-20	21-22	23-24		
		Cerebellum	23-25	26-27	28-29		
		Cortex	20-21	22-23	24-25		

TABLE 3 Recommended maximum required strengths of spherical harmonic (SH) B_0 shim systems for challenging single-voxel locations in human and rodent applications at example B_0 field strengths of 3 and 9.4 T, respectively. Third-order fields for the rodent application were omitted due to a lack of data in the literature. Field units are expressed in Hz/cmⁿ with SH order n, following the conventions in de Graaf and Juchem.⁵ Unit conversion from Hz/cmⁿ to μ T/cmⁿ can be achieved by division by 42.576 Hz/ μ T, employing the Larmor equation for ¹H nuclei. The amplitude of B_0 distortions induced by magnetic susceptibility is proportional to the scanner B_0 field strength. Shim requirements at other fields strengths can be derived employing the rule of proportion, for instance, a 15 Hz/cm² requirement at 3 T corresponds to a 15 Hz/cm² * 7 T/3 T = 35 Hz/cm² requirement at 7 T. Please note that these recommended maximum strengths currently might not be available in all MRI systems

B_0	Application	SH field shape	Max. amplitude
3 T	Human brain ^{5,18,50,51}	X, Y, Z	200 Hz/cm
		X2-Y2, XY	15 Hz/cm ²
		ZX, Z2, ZY	25 Hz/cm ²
		X3, Y3	0.1 Hz/cm ³
		Z(X2-Y2), XYZ	0.3 Hz/cm ³
		Z2X, Z2Y	0.5 Hz/cm ³
		Z3	1.5 Hz/cm ³
9.4 T	Rodent brain ⁴⁹	X, Y, Z	5000 Hz/cm
		X2-Y2, XY	500 Hz/cm ²
		ZX, Z2, ZY	2500 Hz/cm ²

amplitude of B_0 variations induced by nonuniform macroscopic distribution of magnetic susceptibility in and around the subject at hand can be effectively minimized by B_0 shimming.

Details of the B_0 shim procedure are rarely described in scientific publications, rendering their validation by reviewers and reproduction by others difficult. Going forward, it is recommended to summarize defining aspects of the shim analysis along with an overview of the applied SH shim corrections in future MRS publications, either in the Methods section or as an Appendix.

B_0 homogeneity is commonly reported as standard deviation of the residual B_0 distribution, sometimes extended by further measures such as the minimum-maximum range or gradient metrics. In addition to macroscopic B_0 field homogeneity, achievable linewidths also rely on the tissue's magnetic microenvironment and are therefore specific to individual brain and body regions. For MRS/MRSI, the effective spectral linewidth of water and other singlet resonances is therefore quantified directly as the most relevant immediate outcome measure. For quality assurance of B_0 shimming it is recommended to supply a water linewidth report for the defined MRS volume and to show the shim VOI and a related water spectrum or histogram. For whole-brain or organ shimming as required for MRSI the water linewidth would be ideally reported globally but complemented by a B_0 map yielding spatial and local information. In addition, meaningful metabolite linewidths, ie, numeric values, for the application at hand should be reported, such as total creatine at 3 ppm and/or the N-acetylaspartate (NAA) linewidth at 2 ppm for brain MRS/MRSI. Note that natural linewidths differ between molecules and, for instance, the NAA singlet at 2.02 ppm typically exhibits a linewidth 0.5-1.5 Hz narrower than the water linewidth. Also, some apparent singlets, in fact, constitute the sum over two or more resonances, eg, total creatine as the sum of creatine and phosphocreatine at 3.01 and 3.03 ppm, respectively, thereby complicating the interpretation of its FWHM. Besides line broadening, uncompensated B_0 field inhomogeneity can affect the lineshape. A spatial B_0 distribution resembling the shape of the second-order Z2 term, for instance, leads to lineshape asymmetry, which can significantly impact metabolic quantification.

Table 1 and Figure 8 present a summary of attainable B_0 shim quality in humans expressed as water linewidths in different brain and body regions as a function of scanner B_0 magnetic field strength. The water linewidths as an MRS-relevant direct outcome metric of in vivo B_0 shim quality are categorized as excellent, adequate and acceptable for spectral analysis and quantification. It is important to note that the impact of spectral linewidth on quantification accuracy is a complex function of spectral characteristics and overlap with other metabolites,⁵² making the separation between excellent, adequate and acceptable linewidth metabolite-dependent. The PFC is reported separately due to the severe B_0 challenges it experiences, representative for brain regions that are challenging to shim such as the medial temporal lobe or cerebellum. Also, B_0 shim outcome and spectral linewidth are the result of a plurality of methodological choices, for example, the employed SH order and shim VOI. Furthermore, potentially crucial pathological and biological aspects (eg, brain iron content) are not considered. As such, the table aims to provide basic guidance for expectations and assessment of B_0 shim performance in MRS/MRSI studies, but does not claim completeness or general applicability.

Abbreviation: PFC, prefrontal cortex, representative for brain regions that are challenging to shim.

*without iron overload.

A corresponding summary of attainable B_0 shim quality in rodents expressed as water linewidths in different brain regions as a function of scanner B_0 magnetic field strength is presented in Table 2 and Figure 9. As expected, the water linewidth shows an increase with B_0 as the

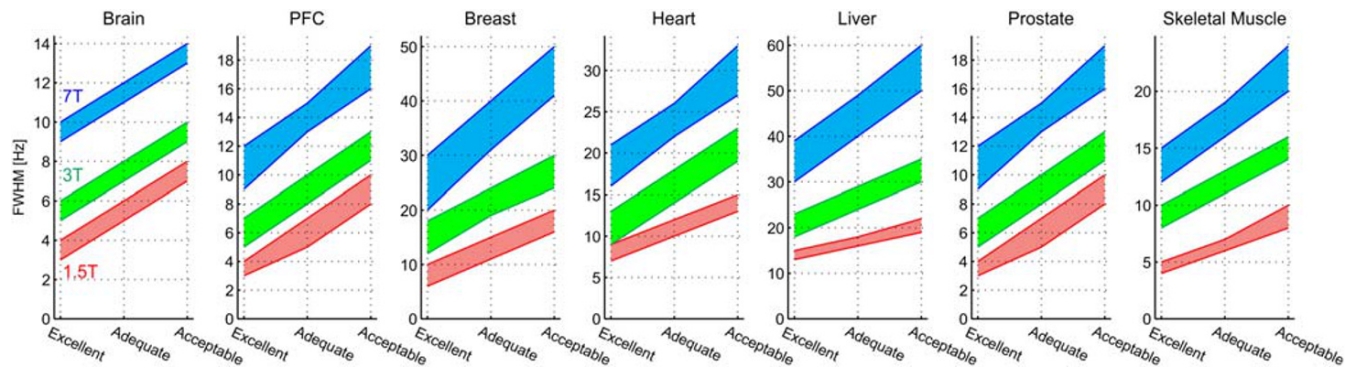


FIGURE 8 Visualization of Table 1, ie, summary of attainable B_0 shim quality expressed as linewidths of the real part water spectrum in humans as a function of scanner B_0 field strength (1.5, 3 and 7 T) and body parts for typical single-voxel acquisitions. Note that this figure is for basic orientation only. PFC, prefrontal cortex

amplitudes of susceptibility-induced B_0 inhomogeneity scales with the B_0 field strength. Similarly, larger shim VOIs containing mixed brain regions (as used typically for X-nuclei MRS) show larger water linewidths due to increased field deformations linked to stronger susceptibility differences between brain regions. Similar to Table 1, biological and pathological aspects beyond basic anatomy are not considered, such as the impact of higher brain water content and less myelin in the early developing brain leading to smaller water linewidths.⁴⁸

9.3 | Automation and clinical workflow

Patient time in the scanner is precious and every effort should be made to fully integrate the B_0 shimming procedures into the clinical workflow, irrespective of whether vendor-provided or customized implementations are used. Furthermore, automation and user independence are considered key for reproducibility across sites and vendors. B_0 shim algorithms should converge quickly and robustly, even if the employed B_0 maps are noisy or contain some minor artifacts. The algorithm should consider respective hardware constraints as well as measured coil fields including cross-terms, rather than assumed theoretical pure ones. This allows the shimming procedure to run in a single iteration, and not require multiple adjustments to iteratively reduce secondary imperfection induced by cross-terms. Manual shimming, especially of higher orders ($n > 1$), should be avoided. However, in the case of very challenging shim problems occurring at large off-center positions for body applications, there should still be an option of a manual repeat for shim improvement or a manual adjustment for validation. The recommended time justifiable for first and second SH order B_0 shimming in human subjects is ~ 1 -2 minutes for single-voxel MRS using projections including the prescription of the shim VOI comprising the MRS voxel. The maximally acceptable time dedicated to B_0 shimming of MRSI including shim VOI selection should not exceed 2-3 minutes for integrated solutions in clinical applications and 4-6 minutes for research applications using work-in-progress packages or stand-alone B_0 shim tools for B_0 shimming of arbitrary SH order.

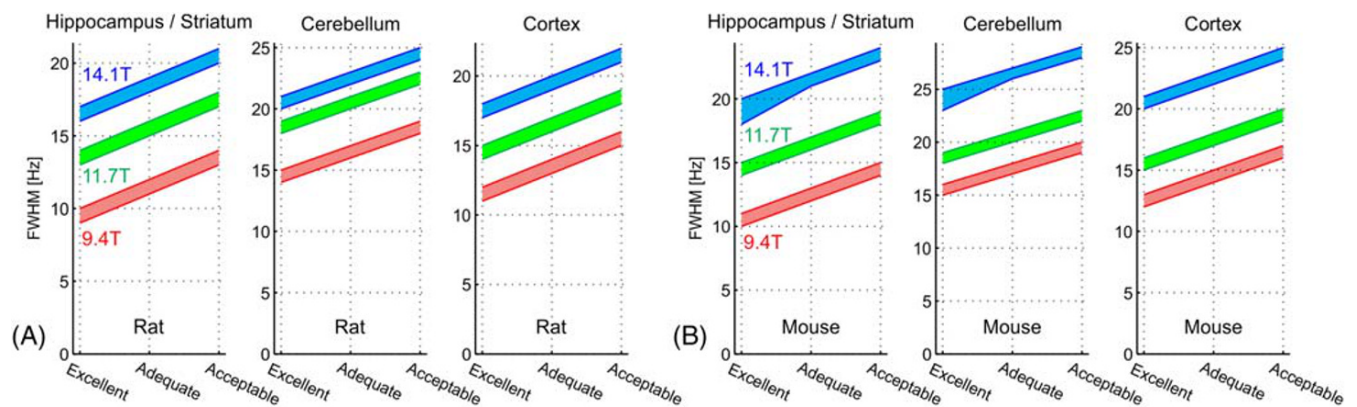


FIGURE 9 Visualization of Table 2, ie, summary of attainable B_0 shim quality expressed as linewidths of the real part water spectrum in rat and mouse brain as a function of scanner B_0 field strength (9.4, 11.7 and 14.1 T) in different brain locations for typical single-voxel acquisitions. Further potentially relevant details are omitted here as they are beyond the scope of this paper. Note that this figure is for basic orientation only

9.4 | Vendor-provided B₀ shim methods and resources

All MR scanners are equipped with B₀ shim capability, but the details can vary substantially. For instance, the calibration of the cross-terms is routinely performed by Bruker. The calibration mechanism is prepared in Philips, but finding appropriate cross-calibration values is up to the user. For other vendors, those and other details remain unknown. In Table 4, a brief overview of the available methods for projection and image-based B₀ shimming for MRS at the time of writing this paper are summarized for the main vendors of preclinical and clinical MR systems as they were made available. Apart from this, both free and commercial third party options are available, of which some freeware options are included in Table 4.

10 | SUMMARY

Excellent B₀ homogeneity is a key requirement for successful MRS and MRSI. High-quality B₀ shimming relies on several factors including reliable methods for B₀ field characterization, high-level experimental calibration of the employed B₀ shim coil hardware, and functional and efficient routines for B₀ field analysis and the calculation of shim coil currents. Several guidelines are presented to achieve B₀ magnetic field homogeneity in humans and rodents, and these are summarized in the following bullet points. Enhanced and consistent B₀ field homogeneity can pave the way for reliable biochemical profiling with MRS and MRSI.

Summary of the major recommendations

- B₀ field shimming methods should provide automatic, robust and high-quality magnetic field homogeneity, although current implementations vary greatly in the degree to which this is achieved.
- Projection-based shimming methods can provide a fast, robust and user-friendly approach for B₀ field shimming in single-voxel MRS but require a spherical ROI for shimming around the MRS voxel.
- Image-based shimming methods can be a suitable alternative for single-voxel MRS, especially with the use of higher than second SH order shimming, and are recommended for MRSI as irregular-shaped ROIs can be taken into account.
- Experimental calibration of shim systems is highly recommended to assure satisfactory shimming results.
- The calculation of shim fields should consider both self- and cross-terms for optimal single-step adjustment of shim currents, thereby mitigating the need for iterations.
- Shim current calculations have to consider the technical limitations, ie, the available dynamic amplitude range, of the shim system at hand.
- Different target organs require tailored shim approaches, both in data acquisition, physiological synchronization and analysis (section 8).
- Procedures and outcomes of B₀ shimming should be reported in future MRS publications as (1) employed SH field shapes and (2) resultant MRS water linewidth (FWHM, mean ± SD for every region), ideally complemented by (3) the metrics of achieved B₀ homogeneity.

ACKNOWLEDGEMENTS

Helpful discussions and contributions to the tables by Drs Ovidiu Andronesi, Patrick Bolan, In-Young Choi, Uzay Emir, Ariane Fillmer, Martin Gajdošík, Lars Hanson, Linda Heskamp, Hermien Kan, Martin Krššák, Andrew Maudsley, Gulin Oz, Jeanine Prompers, Tom Scheenen, Ivan Tkac,

TABLE 4 Overview of the basic availability of different shimming methodologies for the major vendors along with nonvendor freeware tools from the MR community

Vendor	Projection-based shim		Image-based shim	
	provided	nonvendor	provided	nonvendor
Agilent/Varian	no	1, 2	yes	3
Bruker	no		yes	3
Canon	no		linear only	
General Electric	no	2	linear only	3
Philips	yes		yes	4
Siemens	no	5	yes	3

1. Sequence and processing tool available from CMRR (<https://www.cmrr.umn.edu/downloads>)
2. Sequence and processing tool available from Columbia MR SCIENCE Laboratory (http://innovation.columbia.edu/technologies/cu18208_famasito)
3. Sequence and processing tool available from Columbia MR SCIENCE Laboratory (http://innovation.columbia.edu/technologies/cu17326_b0detox)
4. Processing tool available through Philips clinical science (PRIDE)
5. Sequence and processing tool available from CMRR on C2P basis (<https://www.cmrr.umn.edu/downloads>)

Julien Valette and Jannie Wijnen, as well as the ISMRM MR Spectroscopy Study Group, are acknowledged. A further group of experts—recruited by personal invitation, all of them with many years of expertise in the field of B_0 shim methodology—was invited to provide comments and support this publication. The members of this group are listed in Table S1. Financial support was provided by the SNSF project no. 310030_173222/1 and by the CIBM (UNIL, UNIGE, HUG, CHUV, EPFL, as well as the Leenaards and Jeantet Foundations).

ORCID

Christoph Juchem  <https://orcid.org/0000-0002-1505-201X>

Cristina Cudalbu  <https://orcid.org/0000-0003-4582-2465>

Robin A. de Graaf  <https://orcid.org/0000-0002-6570-7010>

Vincent O. Boer  <https://orcid.org/0000-0001-6026-3134>

REFERENCES

1. Oz G, Deelchand DK, Wijnen JP, et al. Advanced single voxel ^1H magnetic resonance spectroscopy techniques in humans: Experts' consensus recommendations [published online ahead of print January 10, 2020]. *NMR Biomed*. <https://doi.org/10.1002/nbm.4236>
2. Maudsley AA, Andronesi OC, Barker PB, et al. Advanced magnetic spectroscopic neuroimaging: Experts' consensus recommendations. *NMR Biomed*. 2020. <https://doi.org/10.1002/nbm.4309>
3. Wilson M, Andronesi O, Barker PB, et al. Methodological consensus on clinical proton MRS of the brain: Review and recommendations. *Magn Reson Med*. 2019;82(2):527-550.
4. Juchem C, de Graaf RA. B_0 magnetic field homogeneity and shimming for in vivo MR spectroscopy. *Anal Biochem*. 2017;529:17-29.
5. de Graaf RA, Juchem C. B_0 Shimming Technology. In: Webb A, ed. *Magnetic Resonance Technology: Hardware and System Component Design*. Cambridge, UK: Royal Society of Chemistry; 2016:166-207.
6. Stockmann JP, Wald LL. In vivo B_0 field shimming methods for MRI at 7T. *Neuroimage*. 2018;168:71-87.
7. Kreis R. Terminology and concepts for the characterization of in vivo MR spectroscopy methods and MR spectra: Background and experts' consensus recommendations. *NMR Biomed*. In press.
8. Tkac I, Andersen P, Adriany G, Merkle H, Ugurbil K, Gruetter R. In vivo ^1H NMR spectroscopy of the human brain at 7 T. *Magn Reson Med*. 2001; 46(3):451-456.
9. Dong Z, Zhang Y, Liu F, Duan Y, Kangarlou A, Peterson BS. Improving the spectral resolution and spectral fitting of $(1) \text{H}$ MRSI data from human calf muscle by the SPREAD technique. *NMR Biomed*. 2014;27(11):1325-1332.
10. Near J, Harris AD, Juchem C, et al. Preprocessing, analysis and quantification in single-voxel magnetic resonance spectroscopy: experts' consensus recommendations [published online ahead of print February 21, 2020]. *NMR Biomed*. 1002/nbm.4257.
11. Juchem C, Merkle H, Schick H, Logothetis NK, Pfeuffer J. Region and volume dependencies in spectral line width assessed by ^1H 2D MR chemical shift imaging in the monkey brain at 7 T. *Magn Reson Imaging*. 2004;22(10):1373-1383.
12. Motyka S, Moser P, Hingerl L, et al. The influence of spatial resolution on the spectral quality and quantification accuracy of whole-brain MRSI at 1.5T, 3T, 7T, and 9.4T. *Magn Reson Med*. 2019;82(2):551-565.
13. Carlsson A, Ljungberg M, Starck G, Forssell-Aronsson E. Degraded water suppression in small volume $(1)\text{H}$ MRS due to localised shimming. *MAGMA*. 2011;24(2):97-107.
14. Boer VO, Andersen M, Lind A, Lee NG, Marsman A, Petersen ET. MR spectroscopy using static higher order shimming with dynamic linear terms (HOS-DLT) for improved water suppression, interleaved MRS-fMRI, and navigator-based motion correction at 7T. *Magn Reson Med*. 2020;84(3): 1101-1112. <https://doi.org/10.1002/mrm.28202>
15. Klose U. In vivo proton spectroscopy in presence of eddy currents. *Magn Reson Med*. 1990;14(1):26-30.
16. Noguchi S. Formulation of the spherical harmonic coefficients of the entire magnetic field components generated by magnetic moment and current for shimming. *J Appl Phys*. 2014;115(16):163908.
17. Juchem C, Nixon TW, Diduch P, Rothman DL, Starewicz P, de Graaf RA. Dynamic shimming of the human brain at 7 Tesla. *Concepts Magn Reson*. 2010;37B(3):116-128.
18. Pan JW, Lo KM, Hetherington HP. Role of high order and degree $B(0)$ shimming for spectroscopic imaging of the human brain at 7 Tesla. *Magn Reson Med*. 2012;68(4):1007-1017.
19. Fillmer A, Vannesjo SJ, Pavan M, Scheidegger M, Pruessmann KP, Henning A. Fast iterative pre-emphasis calibration method enabling third-order dynamic shim updated fMRI. *Magn Reson Med*. 2016;75(3):1119-1131.
20. Schwerter M, Hetherington H, Moon CH, et al. Interslice current change constrained B_0 shim optimization for accurate high-order dynamic shim updating with strongly reduced eddy currents. *Magn Reson Med*. 2019;82(1):263-275.
21. Juchem C, Nixon TW, McIntyre S, Boer VO, Rothman DL, de Graaf RA. Dynamic multi-coil shimming of the human brain at 7 Tesla. *J Magn Reson*. 2011;212:280-288.
22. Truong TK, Darnell D, Song AW. Integrated RF/shim coil array for parallel reception and localized B shimming in the human brain. *Neuroimage*. 2014; 103C:235-240.
23. Stockmann JP, Witzel T, Keil B, et al. A 32-channel combined RF and B_0 shim array for 3T brain imaging. *Magn Reson Med*. 2016;75(1):441-451.
24. Aghaeifar A, Mirkes C, Bause J, et al. Dynamic B_0 shimming of the human brain at 9.4 T with a 16-channel multi-coil shim setup. *Magn Reson Med*. 2018;80(4):1714-1725.
25. Gruetter R, Boesch C. Fast, noniterative shimming of spatially localized signals. In vivo analysis of the magnetic field along axes. *J Magn Reson*. 1992; 96:323-334.
26. Gruetter R. Automatic, localized in vivo adjustment of all first- and second-order shim coils. *Magn Reson Med*. 1993;29(6):804-811.
27. Koch KM, McIntyre S, Nixon TW, Rothman DL, de Graaf RA. Dynamic shim updating on the human brain. *J Magn Reson*. 2006;180(2):286-296.

28. Cusack R, Papadakis N. New robust 3-D phase unwrapping algorithms: application to magnetic field mapping and undistorting echoplanar images. *Neuroimage*. 2002;16(3 Pt 1):754-764.
29. Dagher J, Reese T, Bilgin A. High-resolution, large dynamic range field map estimation. *Magn Reson Med*. 2013;71(1):105-117. <https://doi.org/10.1063/1.487224>
30. Jenkinson M. Fast, automated, N-dimensional phase-unwrapping algorithm. *Magn Reson Med*. 2003;49(1):193-197.
31. Bydder M, Yokoo T, Hamilton G, et al. Relaxation effects in the quantification of fat using gradient echo imaging. *Magn Reson Imaging*. 2008;26(3):347-359.
32. Boer VO, Siero JC, Hoogduin H, van Gorp JS, Luijten PR, Klomp DW. High-field MRS of the human brain at short TE and TR. *NMR Biomed*. 2011;24(9):1081-1088.
33. Boer VO, Luttje MP, Luijten PR, Klomp DW. Requirements for static and dynamic higher order B0 shimming of the human breast at 7 T. *NMR Biomed*. 2014;27(6):625-631.
34. Dixon WT. Simple proton spectroscopic imaging. *Radiology*. 1984;153(1):189-194.
35. Glover GH, Schneider E. Three-point Dixon technique for true water/fat decomposition with B0 inhomogeneity correction. *Magn Reson Med*. 1991;18(2):371-383.
36. Gruetter R, Tkac I. Field mapping without reference scan using asymmetric echo-planar techniques. *Magn Reson Med*. 2000;43(2):319-323.
37. Reynaud O, Gallichan D, Schaller B, Gruetter R. Fast low-specific absorption rate B0-mapping along projections at high field using two-dimensional radiofrequency pulses. *Magn Reson Med*. 2015;73(3):901-908.
38. Shen J, Rycyna RE, Rothman DL. Improvements on an in vivo automatic shimming method [FASTERMAP]. *Magn Reson Med*. 1997;38(5):834-839.
39. Landheer K, Juchem C. FAMASITO - FASTMAP shim tool towards user-friendly single-step B0 homogenization. In *Proc ISMRM. Montreal, QC, Canada*. 2019, p. 216.
40. Klassen LM, Menon RS. Robust automated shimming technique using arbitrary mapping acquisition parameters (RASTAMAP). *Magn Reson Med*. 2004;51(5):881-887.
41. Hetherington HP, Chu WJ, Gonen O, Pan JW. Robust fully automated shimming of the human brain for high-field 1H spectroscopic imaging. *Magn Reson Med*. 2006;56(1):26-33.
42. Smith SM. Fast robust automated brain extraction. *Hum Brain Mapp*. 2002;17(3):143-155.
43. Juchem C, Nixon TW, McIntyre S, Rothman DL, de Graaf RA. Magnetic field homogenization of the human prefrontal cortex with a set of localized electrical coils. *Magn Reson Med*. 2010;63(1):171-180.
44. Fillmer A, Kirchner T, Cameron D, Henning A. Constrained image-based B0 shimming accounting for "local minimum traps" in the optimization and field inhomogeneities outside the region of interest. *Magn Reson Med*. 2015;73(4):1370-1380.
45. Hess AT, Dylan Tisdall M, Andronesi OC, Meintjes EM, van der Kouwe AJ. Real-time motion and B(0) corrected single voxel spectroscopy using volumetric navigators. *Magn Reson Med*. 2011;66:314-323.
46. Keating B, Ernst T. Real-time dynamic frequency and shim correction for single-voxel magnetic resonance spectroscopy. *Magn Reson Med*. 2012;68(5):1339-1345.
47. Boer VO, van de Bank BL, van Vliet G, Luijten PR, Klomp DW. Direct B0 field monitoring and real-time B0 field updating in the human breast at 7 Tesla. *Magn Reson Med*. 2012;67(2):586-591.
48. Tkac I. *Methodology of MRS in Animal Models: Technical Challenges and Solutions*. Switzerland: Springer International Publishing; 2016.
49. Tkac I, Henry PG, Andersen P, Keene CD, Low WC, Gruetter R. Highly resolved in vivo 1H NMR spectroscopy of the mouse brain at 9.4 T. *Magn Reson Med*. 2004;52(3):478-484.
50. Prinsen H, de Graaf RA, Mason GF, Pelletier D, Juchem C. Reproducibility measurement of glutathione, GABA, and glutamate: Towards in vivo neurochemical profiling of multiple sclerosis with MR spectroscopy at 7T. *J Magn Reson Imaging*. 2017;45(1):187-198.
51. Clare S, Evans J, Jezzard P. Requirements for room temperature shimming of the human brain. *Magn Reson Med*. 2005;55(1):210-214.
52. Near J, Harris AD, Juchem C, et al. Preprocessing, analysis and quantification in single-voxel magnetic resonance spectroscopy: Experts' consensus recommendations. *NMR Biomed*, In press. <https://doi.org/10.1002/nbm.4257>
53. Traber F, Block W, Freymann N, et al. A multicenter reproducibility study of single-voxel 1H-MRS of the medial temporal lobe. *Eur Radiol*. 2006;16(5):1096-1103.
54. Bolan PJ, Kim E, Herman BA, et al. MR spectroscopy of breast cancer for assessing early treatment response: Results from the ACRIN 6657 MRS trial. *J Magn Reson Imaging*. 2017;46(1):290-302.
55. Weiss K, Martini N, Boesiger P, Kozerke S. Cardiac proton spectroscopy using large coil arrays. *NMR Biomed*. 2013;26(3):276-284.
56. van der Meer RW, Doornbos J, Kozerke S, et al. Metabolic imaging of myocardial triglyceride content: reproducibility of 1H MR spectroscopy with respiratory navigator gating in volunteers. *Radiology*. 2007;245(1):251-257.
57. Heerschap A, Jager GJ, van der Graaf M, Barentsz JO, Ruijs SH. Proton MR spectroscopy of the normal human prostate with an endorectal coil and a double spin-echo pulse sequence. *Magn Reson Med*. 1997;37(2):204-213.
58. Gao F, Bottomley PA, Arnold C, Weiss RG. The effect of orientation on quantification of muscle creatine by 1H MR spectroscopy. *Magn Reson Imaging*. 2003;21(5):561-566.
59. Krssak M, Lindeboom L, Schrauwen-Hinderling V, et al. Proton magnetic resonance spectroscopy in skeletal muscle: Experts' consensus recommendations [published online ahead of print February 5, 2020]. *NMR Biomed*. <https://doi.org/10.1002/nbm.4266>
60. Deelchand DK, Berrington A, Noeske R, et al. Across-vendor standardization of semi-LASER for single-voxel MRS at 3T [published online ahead of print December 18, 2019]. *NMR Biomed*. <https://doi.org/10.1002/nbm.4218>
61. Schaller B, Xin L, Cudalbu C, Gruetter R. Quantification of the neurochemical profile using simulated macromolecule resonances at 3 T. *NMR Biomed*. 2013;26(5):593-599.
62. Krssak M, Reiter G, Chmelik M, et al. Assessment of myocardial lipid accumulation: Optimisation of in vivo 1H magnetic resonance spectroscopy (MRS) measurement protocol. *Proc ESMRMB*. Lisbon, Portugal; 2012, 724.
63. Fillmer A, Hock A, Cameron D, Henning A. Non-water-suppressed ¹H MR spectroscopy with orientational prior knowledge shows potential for separating intra- and extramyocellular lipid signals in human myocardium. *Sci Rep*. 2017;7(1):16898.

64. Machann J, Bongers M, Fritsche A, et al. 1H-MRS of the Myocardium at 3T Applying a 60-Channel Body Array Coil – Initial Experiences. Proc ISMRM. Singapore; 2016, 1098.
65. Krssak M, Hofer H, Wrba F, et al. Non-invasive assessment of hepatic fat accumulation in chronic hepatitis C by 1H magnetic resonance spectroscopy. *Eur J Radiol.* 2010;74(3):e60-e66.
66. Hock A, Valkovic L, Geier A, Kuntzen T, Boesiger P, Henning A. Navigator based respiratory gating during acquisition and preparation phases for proton liver spectroscopy at 3 T. *NMR Biomed.* 2014;27(3):348-355.
67. Basharat M, Payne GS, Morgan VA, Parker C, Dearnaley D, deSouza NM. TE = 32 ms vs TE = 100 ms echo-time ¹H-magnetic resonance spectroscopy in prostate cancer: Tumor metabolite depiction and absolute concentrations in tumors and adjacent tissues. *J Magn Reson Imaging.* 2015;42(4):1086-1093.
68. Gajdosik M, Chadzynski GL, Hangel G, et al. Ultrashort-TE stimulated echo acquisition mode (STEAM) improves the quantification of lipids and fatty acid chain unsaturation in the human liver at 7 T. *NMR Biomed.* 2015;28(10):1283-1293.
69. Tayari N, Heerschap A, Scheenen TWJ, Kobus T. In vivo MR spectroscopic imaging of the prostate, from application to interpretation. *Anal Biochem.* 2017;529:158-170.
70. Klepochova R, Valkovic L, Gajdosik M, et al. Detection and alterations of acetylcarnitine in human skeletal muscles by 1H MRS at 7 T. *Invest Radiol.* 2017;52(7):412-418.
71. Braissant O, Rackayova V, Pierzchala K, Grosse J, McLin VA, Cudalbu C. Longitudinal neurometabolic changes in the hippocampus of a rat model of chronic hepatic encephalopathy. *J Hepatol.* 2019;71(3):505-515.
72. Tkac I, Rao R, Georgieff MK, Gruetter R. Developmental and regional changes in the neurochemical profile of the rat brain determined by in vivo 1H NMR spectroscopy. *Magn Reson Med.* 2003;50(1):24-32.
73. Rackayova V, Braissant O, McLin VA, Berset C, Lanz B, Cudalbu C. ¹H and ³¹P magnetic resonance spectroscopy in a rat model of chronic hepatic encephalopathy: in vivo longitudinal measurements of brain energy metabolism. *Metab Brain Dis.* 2016;31(6):1303-1314.
74. Iltis I, Koski DM, Eberly LE, et al. Neurochemical changes in the rat prefrontal cortex following acute phencyclidine treatment: an in vivo localized ¹H MRS study. *NMR Biomed.* 2009;22(7):737-744.
75. de Graaf RA, Brown PB, McIntyre S, Nixon TW, Behar KL, Rothman DL. High magnetic field water and metabolite proton T1 and T2 relaxation in rat brain in vivo. *Magn Reson Med.* 2006;56(2):386-394.
76. Wang WT, Lee P, Yeh HW, Smirnova IV, Choi IY. Effects of acute and chronic hyperglycemia on the neurochemical profiles in the rat brain with streptozotocin-induced diabetes detected using in vivo ¹H MR spectroscopy at 9.4 T. *J Neurochem.* 2012;121(3):407-417.
77. Choi IY, Lee P, Wang WT, et al. Metabolism changes during aging in the hippocampus and striatum of glud1 (glutamate dehydrogenase 1) transgenic mice. *Neurochem Res.* 2014;39(3):446-455.
78. Tkac I, Dubinsky JM, Keene CD, Gruetter R, Low WC. Neurochemical changes in Huntington R6/2 mouse striatum detected by in vivo 1H NMR spectroscopy. *J Neurochem.* 2007;100(5):1397-1406.
79. Rizzo F, Abaei A, Nespoli E, et al. Aripiprazole and riluzole treatment alters behavior and neurometabolites in young ADHD rats: a longitudinal ¹H-NMR spectroscopy study at 11.7T. *Transl Psychiatry.* 2017;7(8):e1189.
80. Rizzo F, Nespoli E, Abaei A, et al. Aripiprazole selectively reduces motor tics in a young animal model for Tourette's Syndrome and Comorbid Attention Deficit and Hyperactivity Disorder. *Front Neurol.* 2018;9:59.
81. Janssen CI, Zerbi V, Mutsaers MP, et al. Effect of perinatally supplemented flavonoids on brain structure, circulation, cognition, and metabolism in C57BL/6J mice. *Neurochem Int.* 2015;89:157-169.
82. Pepin J, Francelle L, Carrillo-de Sauvage MA, et al. In vivo imaging of brain glutamate defects in a knock-in mouse model of Huntington's disease. *Neuroimage.* 2016;139:53-64.
83. Ligneul C, Palombo M, Hernandez-Garzon E, et al. Diffusion-weighted magnetic resonance spectroscopy enables cell-specific monitoring of astrocyte reactivity in vivo. *Neuroimage.* 2019;191:457-469.
84. Xin L, Gambarota G, Cudalbu C, Mlynarik V, Gruetter R. Single spin-echo T2 relaxation times of cerebral metabolites at 14.1 T in the in vivo rat brain. *MAGMA.* 2013;26(6):549-554.
85. Cudalbu C, Mlynarik V, Xin L, Gruetter R. Comparison of T1 relaxation times of the neurochemical profile in rat brain at 9.4 Tesla and 14.1 Tesla. *Magn Reson Med.* 2009;62(4):862-867.
86. Cudalbu C, Craveiro M, Mlynarik V, Bremer J, Aguzzi A, Gruetter R. In vivo longitudinal ¹H MRS study of transgenic mouse models of prion disease in the hippocampus and cerebellum at 14.1 T. *Neurochem Res.* 2015;40(12):2639-2646.
87. Cudalbu C, McLin VA, Lei H, et al. The C57BL/6J mouse exhibits sporadic congenital portosystemic shunts. *PLoS ONE.* 2013;8(7):e69782.
88. Lai M, Vassallo I, Lanz B, et al. In vivo characterization of brain metabolism by ¹H MRS, ¹³C MRS and ¹⁸F FDG PET reveals significant glucose oxidation of invasively growing glioma cells. *Int J Cancer.* 2018;143(1):127-138.
89. Craveiro M, Clement-Schatlo V, Marino D, Gruetter R, Cudalbu C. In vivo brain macromolecule signals in healthy and glioblastoma mouse models: 1H magnetic resonance spectroscopy, post-processing and metabolite quantification at 14.1 T. *J Neurochem.* 2014;129(5):806-815.
90. Lai M, Lanz B, Poitry-Yamate C, et al. In vivo ¹³C MRS in the mouse brain at 14.1 Tesla and metabolic flux quantification under infusion of [1,6-(13)C2]glucose. *J Cereb Blood Flow Metab.* 2018;38(10):1701-1714.

SUPPORTING INFORMATION

Additional supporting information may be found online in the Supporting Information section at the end of this article.

How to cite this article: Juchem C, Cudalbu C, de Graaf RA, et al. B₀ shimming for in vivo magnetic resonance spectroscopy: Experts' consensus recommendations. *NMR in Biomedicine.* 2020;e4350. <https://doi.org/10.1002/nbm.4350>